Importance of effective dimensionality in manganese pnictides

Manuel Zingl,[1,*] Elias Assmann,[1] Priyanka Seth,[2] Igor Krivenko,[3] and Markus Aichhorn[1]
[1]*Institute of Theoretical and Computational Physics, Graz University of Technology, NAWI Graz, 8010 Graz, Austria*
[2]*Institut de Physique Théorique (IPhT), CEA, CNRS, UMR CNRS 3681, 91191 Gif-sur-Yvette, France*
[3]*Institut für Theoretische Physik, Uni. Hamburg, Jungiusstraße 9, 20355 Hamburg, Germany*
(Received 16 March 2016; revised manuscript received 29 June 2016; published 21 July 2016)

In this paper we investigate the two manganese pnictides $BaMn_2As_2$ and LaMnAsO, using fully charge self-consistent density functional plus dynamical mean-field theory calculations. These systems have a nominally half-filled *d* shell, and as a consequence, electronic correlations are strong, placing these compounds at the verge of a metal-insulator transition. Although their crystal structure is composed of similar building blocks, our analysis shows that the two materials exhibit a very different effective dimensionality, LaMnAsO being a quasi-two-dimensional material in contrast to the much more three-dimensional $BaMn_2As_2$. We demonstrate that the experimentally observed differences in the Néel temperature, the band gap, and the optical properties of the manganese compounds under consideration can be traced back to exactly this effective dimensionality. Our calculations show excellent agreement with measured optical spectra.

DOI: 10.1103/PhysRevB.94.045130

I. INTRODUCTION

The Mott phenomenon, the occurrence of an insulating state solely due to electronic correlations, is among the most intensively studied effects in correlated solid state physics [1]. This insulating state can occur in situations where simple band theory would not allow it, e.g., for an odd number of electrons per unit cell in the absence of symmetry breaking. It is interesting not only in its own right but also as it is the host for other fascinating phenomena, the best-known example being high temperature superconductivity in cuprate oxides. There, injecting charge carriers into this Mott insulating state by chemical doping creates a non-Fermi-liquid state which becomes superconducting at low temperatures [2].

In recent years another class of high-temperature superconductors, the iron-based pnictide and chalcogenide materials, has been identified [3]. In contrast to the cuprates, they are intrinsically multiband systems with the whole 3*d* manifold being relevant for the electronic properties [4,5]. These iron-based materials share common building blocks, the iron-pnictogen or iron-chalcogen layers, and a nominal electronic configuration of six electrons in the five Fe-3*d* bands, which places them in the "Hund's metal" regime [6–8]. As a result of this band filling, these materials have very low coherence scales and sizable correlations, without, however, being close to a Mott metal-insulator transition.

Since superconductivity arises from quantum fluctuations in the normal state, we must understand the physical properties of the relevant parent compounds before we can hope to understand superconductivity. In this paper we therefore investigate the two *manganese* pnictide compounds $BaMn_2As_2$ and LaMnAsO, which are isostructural to the iron-based superconductors $BaFe_2As_2$ and LaFeAsO, but host only five electrons in the five Mn-3*d* bands. These systems can be seen as the pnictide analog of the undoped parent compounds of the cuprate high-temperature superconductors [9,10]. The half-filled Mn-3*d* shells of these compounds promote Mott physics [11–13]. Efforts to induce metallicity by pressure [14] or doping [15–21] have been to some extent successful. While no superconducting state has been demonstrated conclusively [14], the manganese pnictides still feature fascinating properties such as giant magnetoresistance [22,23], large Seebeck coefficients [24–27], and strongly enhanced magnetism with antiferromagnetic (AFM) order persisting up to elevated temperatures [23,28]. In contrast to the related iron pnictides, both manganese pnictides investigated here are semiconductors, as shown in optical and conductivity measurements [11,14,17,25–27,29–31].

When considering an insulating state in a half-filled system the question arises whether this state occurs due to electronic correlations alone (Mott mechanism) or because of symmetry breaking such as magnetism (Slater mechanism). In many correlated materials both mechanisms are at work and sometimes are of similar importance. Furthermore, it has been shown that the proximity to a Mott transition can strongly increase the magnetic ordering temperature [32]. For instance, 1111 manganese pnictides including LaMnAsO ($T_N \approx 350$ K [22,24,33]) and some 122 manganese pnictides, like $BaMn_2P_2$ ($T_N > 750$ K [34]) and $BaMn_2As_2$ ($T_N = 625$ K [28]), remain ordered well above room temperature. Néel temperatures of this order naturally call for a closer investigation of the underlying mechanisms.

We will show that LaMnAsO and $BaMn_2As_2$ are both close to a metal-insulator transition. However, there are differences in the effective dimensionality of the two compounds, which will turn out to be decisive for their properties. Specifically, $BaMn_2As_2$ crystallizes in a $ThCr_2Si_2$-type structure and shows G-type AFM (antiferromagnetic in all directions, see Fig. 1 right) and a large magnetic moment of 3.9 μ_B/Mn [28]. LaMnAsO, with its ZrCuSiAs structure, features antiferromagnetic Mn planes with a magnetic moment of 3.6 μ_B/Mn [23,35], but the coupling between planes is ferromagnetic (C-type AFM, shown in Fig. 1 left). Although both compounds share Mn-As layers with comparable Mn-Mn distances, the different layer stacking and the larger Mn interlayer spacing turn LaMnAsO into a quasi-two-dimensional compound [33,36,37], while $BaMn_2As_2$ is much more three dimensional [26,38]. A dependence of the physical properties on the effective

*manuel.zingl@tugraz.at

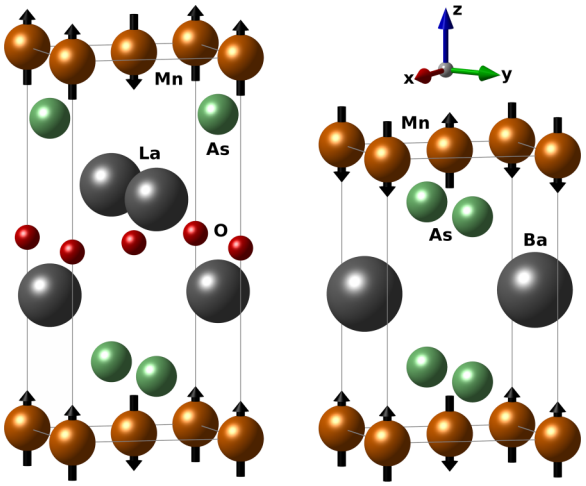

FIG. 1. Crystal and magnetic structure of LaMnAsO (left) and $BaMn_2As_2$ (right) drawn with VESTA [41]. The black arrows represent the Mn spins in the antiferromagnetic states of LaMnAsO [23] (C-type: ferromagnetically stacked antiferromagnetic planes) and $BaMn_2As_2$ [28] (G-type: alternating in all directions). We choose a coordinate system where the x and y axes point towards the nearest-neighbor Mn atoms.

dimensionality has also been observed, e.g., in the iron pnictides [39,40].

This paper is organized as follows. Section II is dedicated to an outline of the methods and parameters we use. In Sec. III, our results on the electronic structure, magnetic, and optical properties are presented and compared to experimental values where available. Finally, we conclude in Sec. IV.

II. METHODS

DFT+DMFT [42], the combination of density functional theory (DFT) and dynamical mean-field theory (DMFT) [43–46], is used as a theoretical framework for the electronic structure calculations presented in this paper. Unless otherwise stated, calculations were carried out with the fully charge self-consistent implementation of the TRIQS/DFTTools package (v1.3) [5,47,48], which is based on Wien2k (v14.2) [49] and the TRIQS library (v1.3) [50]. We use crystal structures measured at 300 K for $BaMn_2As_2$ [28] and 290 K for LaMnAsO [22]. The same crystal structures are used for antiferromagnetic and paramagnetic calculations as no structural phase transition accompanies the magnetic transition in either compound [23,28]. For the antiferromagnetic calculations we use the experimentally determined magnetic orderings (see Fig. 1), which are also predicted by total-energy DFT calculations [26,36]. Note that due to the G-type ordering the magnetic unit cell is doubled in the z direction in $BaMn_2As_2$. For the DFT part of the fully charge self-consistent calculations we use $10000\,k$ points in the full Brillouin zone (BZ) and employ the standard Perdew-Burke-Ernzerhof (PBE) [51] generalized gradient approximation (GGA) for the exchange-correlation functional.

From the DFT Bloch states we construct projective Wannier functions for the Mn-3d orbitals in an energy window from -5.00 eV to 3.40 eV for $BaMn_2As_2$. Likewise, we choose a window from -5.50 eV to 3.25 eV for LaMnAsO. Using such a large energy window for the projections results in a much better localization of the Mn-3d Wannier functions [5,47,52], which plays to the strengths of the DMFT approximation.

In DMFT we work with a full rotationally invariant Slater Hamiltonian for the five Mn-3d orbitals with a Coulomb interaction $U = F^0$ of 5.0 eV and a Hund's coupling $J = (F^2 + F^4)/14$ of 0.9 eV ($F^4/F^2 = 0.625$). We estimate our interaction parameters from the values used in iron pnictide calculations [4,48,53], increasing them slightly to account for the stronger correlations expected in Mn compounds. It is established that the physics of the nominally half filled Mn-3d shells is strongly governed by J [7,8]. We find that our J is consistent with values used in other recent works on manganese pnictides [11,12,54].

Due to the localized nature of the compounds and the substantial electron-electron correlations we choose the fully localized limit (FLL) as double counting correction [55]. In general the choice of the double counting is less crucial in fully charge self-consistent calculations [48].

The TRIQS/CTHYB solver (v1.3) [56], which is based on continuous-time quantum Monte Carlo in the hybridization expansion [57,58], is used to obtain the solution of the impurity model on the Matsubara axis at an inverse temperature $\beta = 40\ \mathrm{eV}^{-1}$, corresponding to room temperature. We use the stochastic maximum entropy method [59] for the analytic continuation of the self-energy to the real-frequency axis. In the antiferromagnetic case the DFT part is performed without spin polarization; thus the magnetic splitting of the Mn-3d spins is purely introduced by DMFT. To describe the desired antiferromagnetic state, the same self-energy is taken for both Mn atoms in the unit cell, but with swapped spins.

We calculate the optical properties within the Kubo formalism, neglecting vertex corrections (strongly suppressed in DMFT [45,60]), as implemented in the TRIQS/DFTTools package [47]. For the optical calculations we increase the number of k points to 150000 for $BaMn_2As_2$ and 100000 for LaMnAsO in the full BZ. The frequency-dependent optical conductivity is given by

$$\sigma^{\alpha\beta}(\Omega) = N_\sigma \pi e^2 \hbar \int d\omega\, \Gamma^{\alpha\beta}(\omega+\Omega,\omega) \times \frac{f(\omega) - f(\omega+\Omega)}{\Omega}, \quad (1)$$

with the spin degeneracy N_σ, the Fermi function $f(\omega)$, and the transport distribution

$$\Gamma^{\alpha\beta}(\omega_1,\omega_2) = \frac{1}{V}\sum_{\mathbf{k}} \mathrm{tr}[v^\alpha(\mathbf{k})A(\mathbf{k},\omega_1)v^\beta(\mathbf{k})A(\mathbf{k},\omega_2)], \quad (2)$$

where V is the unit cell volume. The summation over k points is properly normalized with respect to their weights. The velocities $v^\alpha(\mathbf{k})$, which are proportional to the matrix elements of the momentum operator in direction $\alpha = \{x,y,z\}$, are calculated with the `optic` module of Wien2k [61]. In multiband systems the velocities $v^\alpha_{ij}(\mathbf{k})$ and the spectral function $A_{ij}(\mathbf{k},\omega)$ are Hermitian matrices in the band indices i,j. To analyze the influence of structural differences, we construct maximally localized Wannier functions and real-space Hamiltonians with the help of wien2wannier [62] and Wannier90 [63].

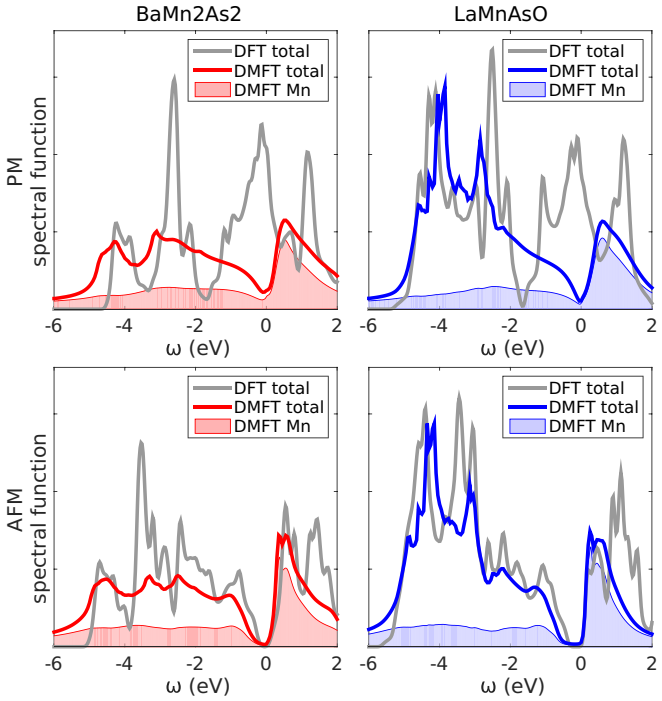

FIG. 2. DFT+DMFT paramagnetic (top row) and antiferromagnetic (bottom row) spectral functions of $BaMn_2As_2$ (red) and LaMnAsO (blue) compared to DFT (gray). The shaded areas correspond to the Mn-projected spectral functions. The Fermi level is set to $\omega = 0$ eV.

III. RESULTS

A. Electronic structure

In this section we present our DFT+DMFT results. While we focus on the antiferromagnetic (AFM) phase, we also consider the paramagnetic (PM) solution to gain insight into the origin of the insulating state (Mott or Slater mechanism).

We start our discussion with the PM spectral functions in Fig. 2 (top). In DFT, the total non-spin-polarized DFT spectral functions (light gray lines) in both compounds are clearly metallic, in contrast to DFT+DMFT, where the weight at the Fermi level is drastically reduced, nearly opening a gap. The structure of the correlated Mn-3d spectral function (shaded areas in Fig. 2) is very similar in both compounds and consists of a heavily smeared-out contribution below the Fermi energy, which shows strong hybridization with the As-4p bands along its full width of about 5.0 eV, and a sharp peak ranging from 0.0 eV to about 2.0 eV. On the other hand, the total spectral functions (thick lines in Fig. 2) differ below -2.0 eV due to oxygen states present in LaMnAsO but not in $BaMn_2As_2$.

The strong electron-electron correlations in the half-filled Mn-3d shells place both compounds near the Mott metal-insulator transition. This is also seen in the k-resolved paramagnetic spectral function in Fig. 3. At the Fermi energy, no remnants of DFT bands are observable, indicating that the spectral weight is solely introduced by the imaginary part of the self-energy. This picture is supported by the quasiparticle weights, which are below 0.13 for all orbitals in both compounds. In the orbital-resolved PM spectral functions of the Mn-3d shell (Fig. 4 top row), we observe

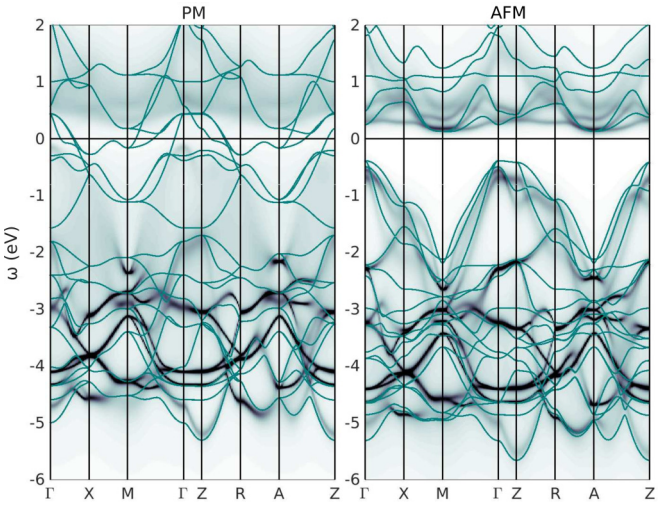

FIG. 3. Spectral function $A(\boldsymbol{k},\omega)$ for the paramagnetic (left) and antiferromagnetic (right) state of LaMnAsO. The thin solid lines show the DFT bands, while the shading shows the DFT+DMFT spectral weight. The Fermi level is set to $\omega = 0$ eV.

orbital-selective behavior: While the $x^2 - y^2$ orbital is still unequivocally metallic, electronic correlations drive the xz, yz, and z^2 orbitals close to the insulating phase. The xy orbital is even more correlated.

To substantiate our claim that the investigated compounds are close to a Mott transition we perform additional calculations for LaMnAsO. At room temperature and an interaction strength of $U = 6.0$ eV and $J = 1.0$ eV it remains metallic. However, both lower temperature ($\beta = 100\ \text{eV}^{-1}$)

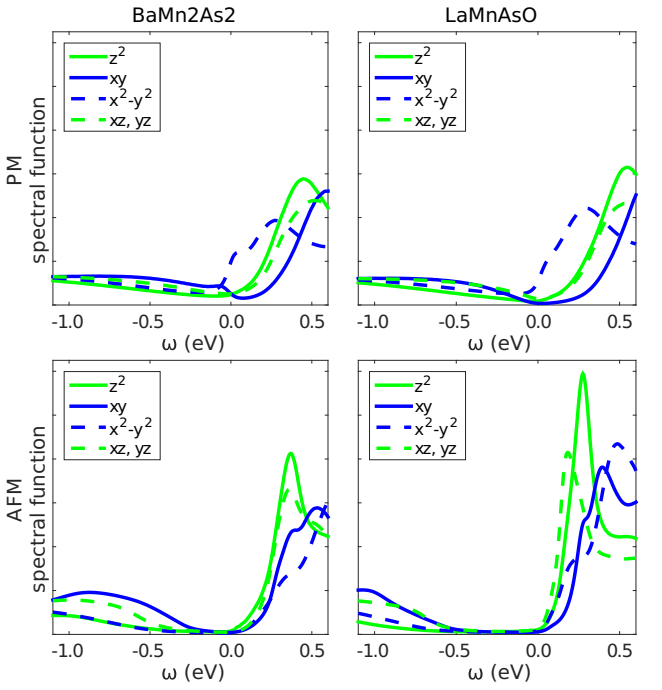

FIG. 4. DFT+DMFT orbital-resolved paramagnetic (top row) and antiferromagnetic (bottom row) spectral functions of the correlated manganese atom for $BaMn_2As_2$ (left) and LaMnAsO (right). The Fermi level is set to $\omega = 0.0$ eV.

and stronger interactions ($U = 7.0$ eV and $J = 1.1$ eV) are independently sufficient to drive the material into the insulating phase. Hence we conclude that our compounds are indeed close to an insulating phase.

It has been shown before that in comparison to $BaFe_2As_2$ electronic correlations have a stronger effect in $BaMn_2As_2$, placing the latter significantly closer to the Mott localization picture [13,64]. Our paramagnetic DFT+DMFT results confirm this observation and extend it to LaMnAsO, which is also more localized than its itinerant Fe relative [5].

Conversely, the AFM spectral functions do feature a gap (Fig. 2 bottom). DFT predicts small gaps of 0.1 eV for $BaMn_2As_2$ and 0.5 eV for LaMnAsO, consistent with earlier theoretical results [17,26,29,36]. In DFT+DMFT, the gap remains similar in $BaMn_2As_2$ but is somewhat enlarged in LaMnAsO, to about 0.6 eV. In the case of $BaMn_2As_2$, the strong incoherence, the finite temperature, and the influence of the analytic continuation prohibit the statement of an exact value for the band gap. Nevertheless, the gap is clearly very narrow in $BaMn_2As_2$ and of the same order as the DFT result.

Although the increase in the band gaps, due to the DFT+DMFT treatment, is smaller than 0.1 eV, electronic correlations lead to important differences in the spectral functions relative to DFT: First, a strong renormalization of the bandwidth of the unoccupied Mn states, and second, a substantial smearing of the occupied Mn spectral weight (see Figs. 2 and 3).

Experiments indicate that $BaMn_2As_2$ has, at least at low temperatures, an indirect band gap of about 0.03 eV [14,27,30,31]. To our knowledge, the only experimental results for the LaMnAsO gap are 1.1 eV from resistivity measurements of a polycrystalline sample at high temperatures [29] and 1.4 eV for LaMnAsO thin films, deduced from optical absorption spectra [25].

In both materials the fundamental gap is indirect, and the smallest direct gap occurs at the Γ point. For $BaMn_2As_2$, this direct gap is about 0.7 eV, close to the recently published value of 0.8 eV [11]. For LaMnAsO, we find a direct gap of about 0.8 eV (see also Fig. 3). Unsurprisingly, the AFM k-resolved spectral function and the indirect/direct gaps of LaMnAsO agree well with DFT+DMFT calculations for the closely related manganese pnictide LaMnPO [54].

Since both compounds share the structure of the Mn-As layers (see Fig. 1), it is natural to ask why the band gap of $BaMn_2As_2$ is narrower. The orbital-resolved AFM DFT+DMFT spectral functions projected on the Mn-3d states (Fig. 4 bottom) reveal that the gap is between the z^2 orbital on the unoccupied side and the xy orbital on the occupied side in $BaMn_2As_2$. On the other hand, in LaMnAsO the xy gap is considerably wider. Therefore, within the assumptions of our calculation, we can attribute the narrower band gap of $BaMn_2As_2$ to the different spectral contributions of the xy and the z^2 orbitals. Interestingly, the structural difference between the investigated compounds mainly impacts those two orbitals, as we will see in the next section.

B. Maximally localized Wannier functions

To understand the influence of the structural differences on the Mn-3d orbitals, and on the resulting physical properties, we construct an effective real-space Hamiltonian for both compounds. For the present section, we set aside the projective Wannier functions we use in DFT+DMFT and construct ten maximally localized Wannier functions from the non-spin-polarized Mn-3d bands. This model has the advantage that it directly provides the effective hopping between Mn atoms, including all hopping paths over intermediate atoms (Ba, La, As, O). Thus, it allows us to compare the two compounds on the same footing. The maximally localized Wannier functions for the Mn-3d orbitals are shown in Fig. 5.

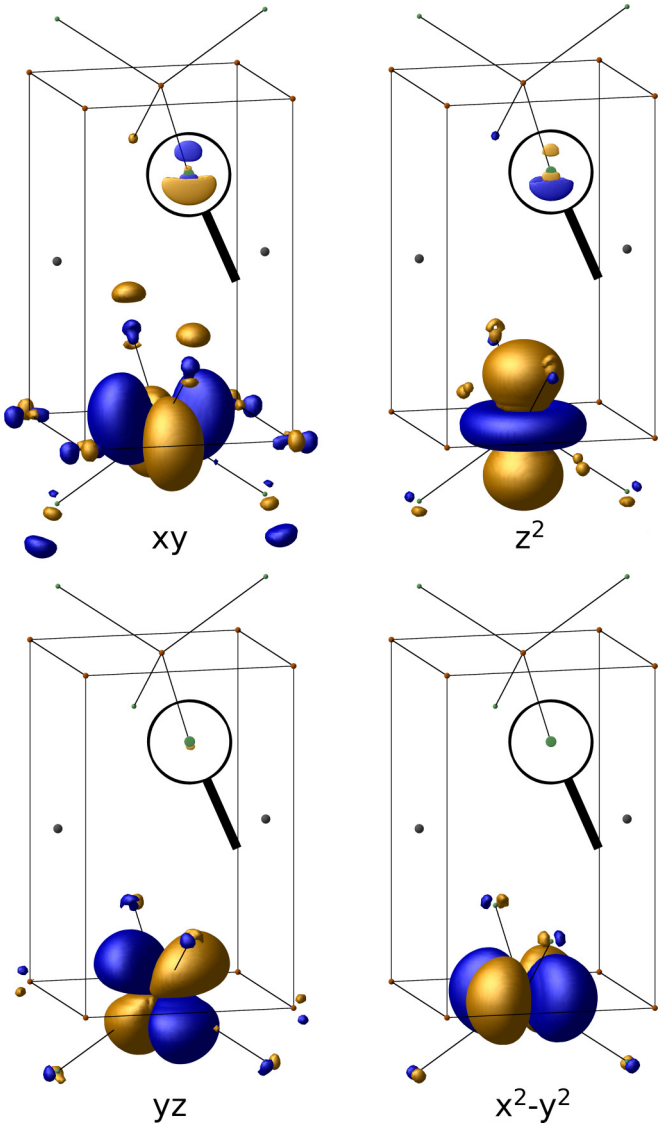

FIG. 5. Real-space representation of the maximally localized Wannier orbitals for the Mn-3d shell of $BaMn_2As_2$ constructed with wien2wannier [62] and Wannier90 [63] and visualized in VESTA [41]. The xz orbital, which is not shown here, is related to the yz orbital by crystal symmetry. The thin lines connect the central Mn atoms to the four nearest As atoms. The xy and z^2 orbitals have significant weight also on the As atoms of the neighboring Mn-As layers. To emphasize this contribution, in the magnifier symbols we show it enlarged both by applying a zoom and selecting a smaller isovalue (by a factor of ten). By contrast, in LaMnAsO, no weight would be seen on the adjacent Mn-As layers at these isovalues.

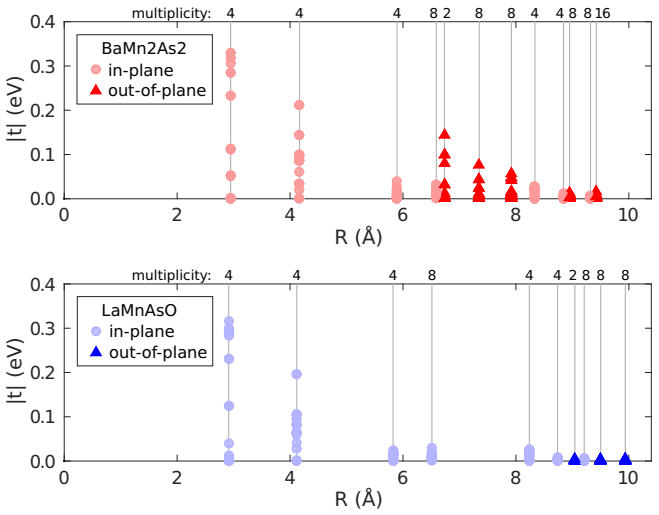

FIG. 6. Real-space Hamiltonian matrix elements $|t|$ for $BaMn_2As_2$ (red) and LaMnAsO (blue) from a Wannier90 construction of the Mn-3d orbitals. Shown are all hoppings between Mn atoms separated by the distance R. The given multiplicities correspond to the number of neighbors at that distance.

The matrix elements of the resulting effective real-space Hamiltonian as a function of distance are plotted in Fig. 6. For each pair of Mn atoms all 25 matrix elements between their five Mn-3d orbitals are shown. Considering the in-plane hopping first (circles), both materials are described by a very similar Hamiltonian, which is expected due to the shared structure of the Mn-As layers and the comparable Mn-Mn distance within those layers. Turning to the interlayer hoppings (triangles), a completely different picture emerges. The Mn atoms in $BaMn_2As_2$ couple substantially to their respective neighbors on adjacent planes, in contrast to LaMnAsO, where the interlayer coupling is on average more than 25 times lower and not visible on the shown scale. From this it follows that LaMnAsO is built up by quasi-two-dimensional Mn-As layers coupled only very weakly to each other, whereas $BaMn_2As_2$ shows much stronger interlayer coupling.

It bears mentioning that in $BaMn_2As_2$ the interlayer hoppings follow a different decay than the in-plane hoppings with distance, as visible in the much stronger coupling for similar atomic distances. The responsible hoppings for the interlayer coupling can be nearly exclusively attributed to the xy and z^2 orbitals, as the coupling of the xz, yz orbitals is already below 0.05 eV. The $x^2 - y^2$ orbitals practically do not contribute to the interlayer coupling. The largest hopping strength is found between the xy orbitals, followed by xy to z^2 and z^2 to z^2.

The difference in the interlayer coupling of the Mn-As layers can be traced back to multiple factors. First, the distance between the Mn-As layers is much shorter in $BaMn_2As_2$ (6.73 Å versus 9.04 Å), where they are separated only by the rather narrow Ba layer in contrast to the thicker La-O layer in LaMnAsO (see Fig. 1). The fact that the in-plane coupling on distances comparable to the interlayer distance is substantially smaller than the out-of-plane coupling indicates that the spatial distance between the layers is not enough to fully explain the enhanced out-of-plane coupling. The second important difference is the stacking inversion of the Mn-As layers in $BaMn_2As_2$. In LaMnAsO the As atoms do not sit directly above each other as they do in $BaMn_2As_2$, where the small As-As distance leads to a simple hopping path via the As atoms. In the maximally localized Wannier functions, this can be seen in the electronic weight of the xy and z^2 orbitals on the As atoms in the adjacent layer (Fig. 5 magnifier symbol).

C. Néel temperature

The highest Néel temperature T_N in a class of compounds is usually found close to the Mott transition. This was first shown for the single-band Hubbard model on the Bethe lattice [65] and the same argument was recently found to be valid for the 4d perovskite $SrTcO_3$ [32] with its exceptionally high transition temperature of 1000 K. When starting from an itinerant picture, for a model with bandwidth W, where the interactions of order U are treated on a mean-field level, the transition temperature scales as $T_N \sim \exp(-W/U)$. On the fully localized side, the adequate picture is the Heisenberg model, where the scaling is $T_N \sim W^2/U$. Between these two extreme cases we can expect a crossover around $U \approx W$, which coincides with the crossover from an itinerant to a localized system. These qualitative considerations identify the Mott transition as a hotspot for magnetism, and hence, materials in this critical region are prone to higher transition temperatures.

From the paramagnetic DFT+DMFT spectral function and the quasiparticle weights, we have seen that $BaMn_2As_2$ and LaMnAsO are close to a Mott transition, and their experimental Néel temperatures are indeed high, with reports of 317 K to 360 K in LaMnAsO [23,33] and even 625 K in $BaMn_2As_2$ [28]. In Fig. 7 we present our DFT+DMFT results for the ordered moment as a function of temperature. For $BaMn_2As_2$ we find an ordering temperature of around 1350 K. Taking into account the overestimation of the transition temperature expected due to the mean-field character of DMFT [32], which is roughly a factor of two [32,66], the prediction of the Néel temperature in our calculation is in reasonable agreement with the experimental value. Also, the

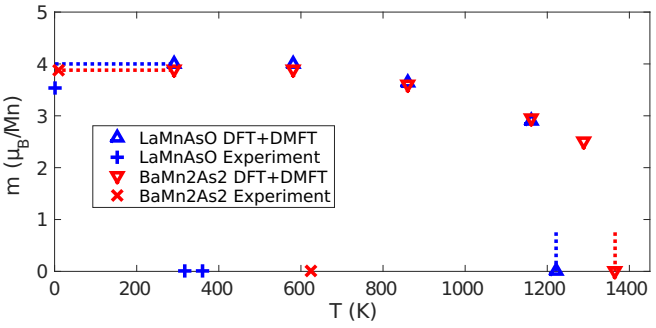

FIG. 7. Magnetic moment m versus temperature T from fully charge self-consistent DFT+DMFT for $BaMn_2As_2$ (red triangles) and LaMnAsO (blue triangles). Experimental points are taken from Refs. [23,33,35] for LaMnAsO (blue crosses) and from Ref. [28] for $BaMn_2As_2$ (red crosses). The horizontal dotted lines mark the saturated magnetic moments and the vertical dotted lines the approximate Néel temperatures.

ordered moment at low temperatures agrees well with the experimental result of 3.9 μ_B/Mn [28].

The situation is different for LaMnAsO. There, the experimental ordering temperature is a factor of two smaller than for $BaMn_2As_2$. However, the DFT+DMFT result is smaller only by about 150 K. This observation is very similar to recent studies in technetium oxides. In the cubic case ($SrTcO_3$), the local DMFT approximation works well [32], but for the layered counterpart Sr_2TcO_4 it overestimates the ordering temperature substantially [67]. The reason is that in quasi-two-dimensional systems, as is the case for Sr_2TcO_4 and also for LaMnAsO, spatial fluctuations become important. They in turn decrease the ordering temperature significantly. In the same way, DFT+DMFT yields a saturated magnetic moment of 4.0 μ_B/Mn in contrast to the measured 3.6 μ_B/Mn [23,35].

From another point of view, it is well known that the strength of the interlayer coupling is a crucial factor influencing the magnetic properties of layered materials [68], for instance in the copper oxides [69,70]. In such compounds, the crossover from a three-dimensional to a layered system leads to a suppression of the Néel temperature, as a function of the interlayer exchange coupling $J_\perp$. As we have observed above, the strong decrease of dimensionality in LaMnAsO is confirmed by a reduction of the hopping in the z direction (by a factor larger than 25). This will also be reflected in an effective $J_\perp$. Band theoretical estimates and experiments suggest that $J_\perp/J_\parallel < 0.015$ in LaMnAsO [36] and $J_\perp/J_\parallel \approx 0.1$ in $BaMn_2As_2$ [38], with $J_\parallel$ being the in-plane nearest neighbor exchange coupling. This supports the conclusion that the reduced Néel temperature in LaMnAsO can be attributed to the lower dimensionality of the system.

D. Optical properties

Finally, we turn to the optical conductivity $\sigma^{\alpha\beta}(\Omega)$, Eq. (1), which will not only exemplify the dimensional differences of the investigated compounds but also allow a comparison with experimental observations. Starting with $BaMn_2As_2$ (Fig. 8 red lines), we observe only a weak anisotropy in the optical conductivity. Besides the depression around $\Omega \approx 2.5$ eV, there is not much of a difference between the in-plane and out-of-plane contributions. This illustrates the more isotropic nature of $BaMn_2As_2$. A small Drude peak present in the in-plane component is in accordance with the observation of a weak metallic behavior at room temperature in Refs. [30,31]. On the contrary, there is no Drude peak in the out-of-plane component, indicating that $BaMn_2As_2$ is insulating along the z direction, in agreement with the optical experiments of Ref. [30]. The optical conductivity of LaMnAsO (Fig. 8 blue lines) in the x direction shows a similar trend, but is reduced by about 1/3 in comparison to $BaMn_2As_2$. Since $\sigma^{zz}(\Omega)$ is strongly suppressed in LaMnAsO, the total optical conductivity becomes largely dominated by the in-plane contribution.

The similar in-plane conductivity of both compounds originates from the common Mn-As layer structure, though the effect of the structural differences becomes apparent in the distinct optical properties in the z direction. We emphasize that the dimensional difference is also visible in the DC conductivity ($\Omega \to 0$). The ratio $\sigma_{xx}(0)/\sigma_{zz}(0)$, an indicator for the anisotropy, is 17 in LaMnAsO but only 7 in $BaMn_2As_2$.

For LaMnAsO the optical conductivity was measured using ellipsometry for a polycrystalline sample [29]. To compare the experimental results to our calculations, we average our theoretical results over all Cartesian directions to obtain a "polycrystalline conductivity" (Fig. 9). In general, the DFT result (solid gray line) follows the trend of the experimental data (black circles), but it severely overestimates the optical conductivity, at some points by more than a factor of two. Similarly, a one-shot DFT+DMFT calculation (dashed blue line), where DMFT is converged without updating the charge density, cannot explain the experimental data. Here, the static spin splitting leads to a larger gap, which is clearly visible in the suppressed optical conductivity below 1.5 eV. Additionally, the unoccupied Mn states are less correlated due to smaller electron-electron scattering as compared to full charge self-consistency. This results in a different distribution of the optical weight.

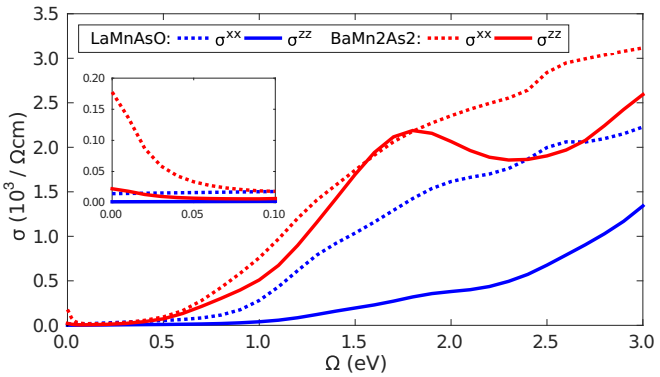

FIG. 8. Optical conductivity tensor components $\sigma^{zz}(\Omega)$ (solid lines) and $\sigma^{xx}(\Omega)$ (dotted lines) of $BaMn_2As_2$ (red) and LaMnAsO (blue) from fully charge self-consistent DFT+DMFT including uncorrelated bands outside the projective window. The inset shows the low frequency region of the optical conductivity in the same units as the main panel.

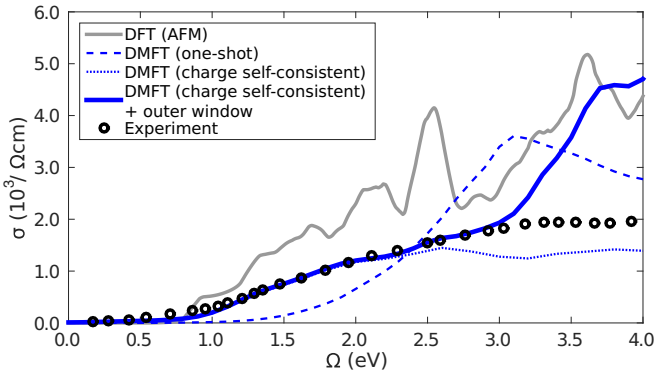

FIG. 9. Optical conductivity of LaMnAsO calculated with DFT (solid gray line), fully charge self-consistent DFT+DMFT in the correlated window (dotted blue line) and including uncorrelated bands (solid blue line) as well as one-shot DFT+DMFT (dashed blue line); compared to experimental data (black circles) from Ref. [29]. Above 3 eV DFT+DMFT (including the outer window) starts to deviate from the experimental data due to the onset of the La-4f bands, which are placed much too low in energy by DFT [55].

On the other hand, in the fully charge self-consistent treatment, the optical results are not only influenced by the modified spectral function but also by the altered velocities of the updated Kohn-Sham bands. Indeed, the fully charge self-consistent DFT+DMFT calculations correctly reproduce the experimental result over a wide range of frequencies (dotted blue line).

The upper limit of our projective energy window is at 3.25 eV, but the chemical potential ($\mu = 1.6$ eV) effectively shifts this level down to 1.65 eV. If we also consider that the Fermi energy is close to the unoccupied states, we see that there can be transitions at $\Omega \approx 2$ eV, which are not captured with our window. Of course this effect sets in very slowly as there are still many other transitions possible at $\Omega \approx 2$ eV. To improve the agreement with experiment, we extend the trace in Eq. (2); now, the spectral function is a matrix built by a block A_{ij} for the correlated bands, as well as blocks for uncorrelated bands below and above the correlated subspace, $A_{\nu\nu'}$. Note that $A_{\nu\nu'} \sim \delta_{\nu\nu'}$ is a noninteracting DFT spectral function. The resulting optical conductivity yields excellent agreement with the experimental data up to about 3 eV (solid blue line). The strong increase above 3 eV is caused by the onset of the La-4f bands, which are known to be placed much too low in energy by DFT [55].

The remarkable agreement with experimental data underlines the importance of the fully charge self-consistent approach and suggests that our choice of the parameters U and J is appropriate. Furthermore, the experimental and theoretical results indicate that the direct band gap of bulk LaMnAsO may be well below the 1.4 eV obtained from thin-film measurements [25].

IV. CONCLUSION

We investigated the manganese pnictides $BaMn_2As_2$ and LaMnAsO in their paramagnetic and antiferromagnetic phases. These manganates represent two points along the dimensional crossover: While $BaMn_2As_2$ is quite isotropic with comparable couplings within and between the Mn-As layers, LaMnAsO is effectively two dimensional with only a weak residual interlayer coupling. This difference, which is already visible in the crystal structure, is substantiated, and its origins are accounted for by the maximally localized Wannier functions for the Mn-3d bands and their hopping amplitudes. We demonstrated that differences in physical properties such as the Néel temperature and DC as well as optical conductivity can be traced back to a large extent to the difference in effective dimensionality.

Our fully charge self-consistent DFT+DMFT calculations yield excellent agreement with the experimental optical conductivity. Our confidence in the applicability of the method to our compounds thus confirmed, we established that both materials are near the Mott metal-insulator transition, which helps explain their high Néel temperatures. Our results constitute an important example where charge self-consistent DFT+DMFT is demonstrably superior to the one-shot approximation.

ACKNOWLEDGMENTS

M. Zingl, E. Assmann, and M. Aichhorn acknowledge financial support from the Austrian Science Fund (Y746, P26220, F04103) as well as NAWI Graz and great hospitality at Collège de France and École Polytechnique. P. Seth acknowledges support from ERC Grant No. 278472-MottMetals. I. Krivenko acknowledges support from Deutsche Forschungsgemeinschaft via Project SFB 668-A3. The authors want to thank E. Schachinger, G. J. Kraberger, and R. Triebl for fruitful discussions. The computational results presented have been achieved using the Vienna Scientific Cluster (VSC) and the dcluster of Graz University of Technology.

[1] M. Imada, A. Fujimori, and Y. Tokura, Rev. Mod. Phys. **70**, 1039 (1998).
[2] P. A. Lee, N. Nagaosa, and X.-G. Wen, Rev. Mod. Phys. **78**, 17 (2006).
[3] Y. Kamihara, T. Watanabe, M. Hirano, and H. Hosono, J. Am. Chem. Soc. **130**, 3296 (2008).
[4] K. Haule, J. H. Shim, and G. Kotliar, Phys. Rev. Lett. **100**, 226402 (2008).
[5] M. Aichhorn, L. Pourovskii, V. Vildosola, M. Ferrero, O. Parcollet, T. Miyake, A. Georges, and S. Biermann, Phys. Rev. B **80**, 085101 (2009).
[6] K. Haule and G. Kotliar, New J. Phys. **11**, 025021 (2009).
[7] A. Georges, L. de' Medici, and J. Mravlje, Annu. Rev. Condens. Matter Phys. **4**, 137 (2013).
[8] L. de' Medici, J. Mravlje, and A. Georges, Phys. Rev. Lett. **107**, 256401 (2011).
[9] H. Ishida and A. Liebsch, Phys. Rev. B **81**, 054513 (2010).
[10] L. de' Medici, G. Giovannetti, and M. Capone, Phys. Rev. Lett. **112**, 177001 (2014).
[11] D. E. McNally, S. Zellman, Z. P. Yin, K. W. Post, H. He, K. Hao, G. Kotliar, D. Basov, C. C. Homes, and M. C. Aronson, Phys. Rev. B **92**, 115142 (2015).
[12] D. E. McNally, J. W. Simonson, K. W. Post, Z. P. Yin, M. Pezzoli, G. J. Smith, V. Leyva, C. Marques, L. DeBeer-Schmitt, A. I. Kolesnikov, Y. Zhao, J. W. Lynn, D. N. Basov, G. Kotliar, and M. C. Aronson, Phys. Rev. B **90**, 180403 (2014).
[13] Y. X. Yao, J. Schmalian, C. Z. Wang, K. M. Ho, and G. Kotliar, Phys. Rev. B **84**, 245112 (2011).
[14] A. T. Satya, A. Mani, A. Arulraj, N. V. C. Shekar, K. Vinod, C. S. Sundar, and A. Bharathi, Phys. Rev. B **84**, 180515 (2011).
[15] A. Pandey, V. K. Anand, and D. C. Johnston, Phys. Rev. B **84**, 014405 (2011).
[16] A. Pandey, R. S. Dhaka, J. Lamsal, Y. Lee, V. K. Anand, A. Kreyssig, T. W. Heitmann, R. J. McQueeney, A. I. Goldman, B. N. Harmon, A. Kaminski, and D. C. Johnston, Phys. Rev. Lett. **108**, 087005 (2012).
[17] J.-K. Bao, H. Jiang, Y.-L. Sun, W.-H. Jiao, C.-Y. Shen, H.-J. Guo, Y. Chen, C.-M. Feng, H.-Q. Yuan, Z.-A. Xu, G.-H. Cao, R. Sasaki, T. Tanaka, K. Matsubayashi, and Y. Uwatoko, Phys. Rev. B **85**, 144523 (2012).
[18] J. Lamsal, G. S. Tucker, T. W. Heitmann, A. Kreyssig, A. Jesche, A. Pandey, W. Tian, R. J. McQueeney, D. C. Johnston, and A. I. Goldman, Phys. Rev. B **87**, 144418 (2013).
[19] A. Pandey and D. C. Johnston, Phys. Rev. B **92**, 174401 (2015).

[20] S. Yeninas, A. Pandey, V. Ogloblichev, K. Mikhalev, D. C. Johnston, and Y. Furukawa, Phys. Rev. B **88**, 241111 (2013).

[21] T. Hanna, S. Matsuishi, K. Kodama, T. Otomo, S.-i. Shamoto, and H. Hosono, Phys. Rev. B **87**, 020401 (2013).

[22] N. Emery, E. J. Wildman, J. M. S. Skakle, G. Giriat, R. I. Smith, and A. C. Mclaughlin, Chem. Commun. **46**, 6777 (2010).

[23] N. Emery, E. J. Wildman, J. M. S. Skakle, A. C. Mclaughlin, R. I. Smith, and A. N. Fitch, Phys. Rev. B **83**, 144429 (2011).

[24] Y.-L. Sun, J.-K. Bao, Y.-K. Luo, C.-M. Feng, Z.-A. Xu, and G.-H. Cao, Europhys. Lett. **98**, 17009 (2012).

[25] K. Kayanuma, H. Hiramatsu, T. Kamiya, M. Hirano, and H. Hosono, J. Appl. Phys. **105**, 073903 (2009).

[26] J. An, A. S. Sefat, D. J. Singh, and M.-H. Du, Phys. Rev. B **79**, 075120 (2009).

[27] D. D. Dung, W. Feng, and S. Cho, J. Vac. Sci. Technol. B **29**, 031210 (2011).

[28] Y. Singh, M. A. Green, Q. Huang, A. Kreyssig, R. J. McQueeney, D. C. Johnston, and A. I. Goldman, Phys. Rev. B **80**, 100403 (2009).

[29] A. Beleanu, J. Kiss, G. Kreiner, C. Köhler, L. Müchler, W. Schnelle, U. Burkhardt, S. Chadov, S. Medvediev, D. Ebke, C. Felser, G. Cordier, B. Albert, A. Hoser, F. Bernardi, T. I. Larkin, D. Pröpper, A. V. Boris, and B. Keimer, Phys. Rev. B **88**, 184429 (2013).

[30] A. Antal, T. Knoblauch, Y. Singh, P. Gegenwart, D. Wu, and M. Dressel, Phys. Rev. B **86**, 014506 (2012).

[31] Y. Singh, A. Ellern, and D. C. Johnston, Phys. Rev. B **79**, 094519 (2009).

[32] J. Mravlje, M. Aichhorn, and A. Georges, Phys. Rev. Lett. **108**, 197202 (2012).

[33] M. A. McGuire and V. O. Garlea, Phys. Rev. B **93**, 054404 (2016).

[34] S. L. Brock, J. Greedan, and S. M. Kauzlarich, J. Solid State Chem. **113**, 303 (1994).

[35] A. C. McLaughlin, private communication (2016). The correct value of the measured manganese magnetic moment in LaMnAsO is 3.55 μ_B/Mn at 2 K, as given in the Supplemental Material of Ref. [23].

[36] S. Dong, W. Li, X. Huang, and E. Dagotto, J. Appl. Phys. **115**, 17D723 (2014).

[37] G. Xu, W. Ming, Y. Yao, X. Dai, S.-C. Zhang, and Z. Fang, Europhys. Lett. **82**, 67002 (2008).

[38] D. C. Johnston, R. J. McQueeney, B. Lake, A. Honecker, M. E. Zhitomirsky, R. Nath, Y. Furukawa, V. P. Antropov, and Y. Singh, Phys. Rev. B **84**, 094445 (2011).

[39] O. Andersen and L. Boeri, Ann. Phys. **523**, 8 (2011).

[40] S. Graser, A. F. Kemper, T. A. Maier, H.-P. Cheng, P. J. Hirschfeld, and D. J. Scalapino, Phys. Rev. B **81**, 214503 (2010).

[41] K. Momma and F. Izumi, J. Appl. Crystallogr. **44**, 1272 (2011).

[42] V. I. Anisimov, A. I. Poteryaev, M. A. Korotin, A. O. Anokhin, and G. Kotliar, J. Phys.: Condens. Matter **9**, 7359 (1997).

[43] W. Metzner and D. Vollhardt, Phys. Rev. Lett. **62**, 324 (1989).

[44] A. Georges and G. Kotliar, Phys. Rev. B **45**, 6479 (1992).

[45] A. Georges, G. Kotliar, W. Krauth, and M. J. Rozenberg, Rev. Mod. Phys. **68**, 13 (1996).

[46] G. Kotliar and D. Vollhardt, Phys. Today **57**, 53 (2004).

[47] M. Aichhorn, L. Pourovskii, P. Seth, V. Vildosola, M. Zingl, O. E. Peil, X. Deng, J. Mravlje, G. J. Kraberger, C. Martins, M. Ferrero, and O. Parcollet, Comput. Phys. Commun. **204**, 200 (2016).

[48] M. Aichhorn, L. Pourovskii, and A. Georges, Phys. Rev. B **84**, 054529 (2011).

[49] P. Blaha, K. Schwarz, G. Madsen, D. Kvasnicka, and J. Luitz, *WIEN2k, An augmented Plane Wave + Local Orbitals Program for Calculating Crystal Properties* (Techn. Universitat Wien, Austria, 2001).

[50] O. Parcollet, M. Ferrero, T. Ayral, H. Hafermann, I. Krivenko, L. Messio, and P. Seth, Comput. Phys. Commun. **196**, 398 (2015).

[51] J. P. Perdew, K. Burke, and M. Ernzerhof, Phys. Rev. Lett. **77**, 3865 (1996).

[52] T. Ribic, E. Assmann, A. Tóth, and K. Held, Phys. Rev. B **90**, 165105 (2014).

[53] S. L. Skornyakov, A. V. Efremov, N. A. Skorikov, M. A. Korotin, Y. A. Izyumov, V. I. Anisimov, A. V. Kozhevnikov, and D. Vollhardt, Phys. Rev. B **80**, 092501 (2009).

[54] J. W. Simonson, Z. P. Yin, M. Pezzoli, J. Guo, J. Liu, K. Post, A. Efimenko, N. Hollmann, Z. Hu, H.-J. Lin, C.-T. Chen, C. Marques, V. Leyva, G. Smith, J. W. Lynn, L. L. Sun, G. Kotliar, D. N. Basov, L. H. Tjeng, and M. C. Aronson, Proc. Natl. Acad. Sci. **109**, E1815 (2012).

[55] M. T. Czyżyk and G. A. Sawatzky, Phys. Rev. B **49**, 14211 (1994).

[56] P. Seth, I. Krivenko, M. Ferrero, and O. Parcollet, Comput. Phys. Commun. **200**, 274 (2016).

[57] P. Werner, A. Comanac, L. de' Medici, M. Troyer, and A. J. Millis, Phys. Rev. Lett. **97**, 076405 (2006).

[58] P. Werner and A. J. Millis, Phys. Rev. B **74**, 155107 (2006).

[59] K. S. D. Beach, arXiv:cond-mat/0403055.

[60] J. M. Tomczak and S. Biermann, Phys. Rev. B **80**, 085117 (2009).

[61] C. Ambrosch-Draxl and J. O. Sofo, Comput. Phys. Commun. **175**, 1 (2006).

[62] J. Kuneš, R. Arita, P. Wissgott, A. Toschi, H. Ikeda, and K. Held, Comput. Phys. Commun. **181**, 1888 (2010).

[63] A. A. Mostofi, J. R. Yates, Y.-S. Lee, I. Souza, D. Vanderbilt, and N. Marzari, Comput. Phys. Commun. **178**, 685 (2008).

[64] P. Werner, M. Casula, T. Miyake, F. Aryasetiawan, A. J. Millis, and S. Biermann, Nat. Phys. **8**, 331 (2012).

[65] M. J. Rozenberg, G. Kotliar, and X. Y. Zhang, Phys. Rev. B **49**, 10181 (1994).

[66] A. I. Lichtenstein, M. I. Katsnelson, and G. Kotliar, Phys. Rev. Lett. **87**, 067205 (2001).

[67] A. Horvat, L. Pourovskii, M. Aichhorn, and J. Mravlje, arXiv:1501.03033.

[68] R. P. Singh and M. Singh, Phys. Status Solidi B **169**, 571 (1992).

[69] R. P. Singh, Z. C. Tao, and M. Singh, Phys. Rev. B **46**, 1244 (1992).

[70] Ajay, S. Patra, and R. S. Tripathi, Phys. Status Solidi B **188**, 787 (1995).